

Dissolved oxygen transfer to sediments by sweep and eject motions in aquatic environments

Ben L. O'Connor^{1,2} and Miki Hondzo

Saint Anthony Falls Laboratory, Department of Civil Engineering, University of Minnesota–Twin Cities,
2 Third Avenue SE, Minneapolis, Minnesota 55414

Abstract

Dissolved oxygen (DO) concentrations were quantified near the sediment–water interface to evaluate DO transfer to sediments in a laboratory recirculating flume and open channel under varying fluid-flow conditions. DO concentration fluctuations were observed within the diffusive sublayer, as defined by the time-averaged DO concentration gradient near the sediment–water interface. Evaluation of the DO concentration fluctuations along with detailed fluid-flow characterizations were used to quantify quasi-periodic sweep and eject motions (bursting events) near the sediments. Bursting events dominated the Reynolds shear stresses responsible for momentum and mass fluctuations near the sediment bed. Two independent methods for detecting bursting events using DO concentration and velocity data produced consistent results. The average time between bursting events was scaled with wall variables and was incorporated into a similarity model to describe the dimensionless mass transfer coefficient (Sherwood number, Sh) in terms of the Reynolds number, Re , and Schmidt number, Sc , which described transport in the flow. The scaling of bursting events was employed with the similarity model to quantify DO transfer to sediments and results showed a high degree of agreement with experimental data.

Introduction

Dissolved oxygen (DO) is an important component of natural water that affects overall water quality, biological communities, and ecosystem function. The distribution of DO in aquatic ecosystems is important to aerobic biota that require DO for metabolism and nutrient cycling, because many of these biogeochemical processes occur across a DO gradient from oxic to anoxic conditions. Sediments represent a substantial sink for DO through benthic respiration as well as decay and oxidation of settled detritus. The flux of DO to sediments is controlled by mass transfer and uptake kinetic limitations. For sediments with an appreciable amount of sand- to silt-sized particles and low porosities, the penetration depth of DO into the sediments is between 1 mm and 10 mm because of the rapid DO uptake (Jørgensen and Boudreau 2001). These observations suggest that characterizing fluid-flow conditions that govern the mass transfer of DO to sediments is

crucial to understanding the dynamics of DO in aquatic ecosystems.

Several studies have examined the transport of DO to sediments in estuaries, lakes, and rivers. Using microscale measurements of DO concentration profiles, some studies have demonstrated the existence of a concentration boundary layer just above the sediment–water interface, which is depicted by a sharp decline in the time-averaged DO concentration (Boudreau 2001). Traditionally, the DO flux to sediments has been modeled using the thin-film theory. The bulk water is continuously supplied with DO by atmospheric reaeration and the sediments act as a DO sink. Turbulent mixing results in a uniform DO concentration in the bulk fluid that decreases through a thin-film above the sediments that allows for DO transport by diffusion (Fig. 1). The thickness of the diffusive sublayer (DSL) decreases with increasing flow velocities (Jørgensen and Des Marais 1990); however, there is uncertainty regarding how to quantify the DSL thickness (Steinberger and Hondzo 1999), if molecular diffusion is the only mode of transport or whether dispersion and turbulent diffusion are also important processes (Güss 1998).

A small number of studies have demonstrated temporal fluctuations of DO concentration just above the sediment–water interface that can be linked to fluid-flow conditions (Gundersen and Jørgensen 1990; Lorke et al. 2003; Røy et al. 2004). An alternative model for describing mass transport, which was consistent with these observed temporal fluctuations of DO, was the surface-renewal theory developed by Danckwerts (1951) and more quantitatively described by Pinczewski and Sideman (1974). This model was based upon near-wall, microscopic observations of the flow field from numerous flow visualization experiments from the 1960s and 1970s relating to the periodic, coherent motions observed in turbulent flows (Robinson 1991). Mass and momentum fluxes occurred through a developing boundary layer (in the streamwise x -

¹ Corresponding author (boconnor@usgs.gov).

² Present address: U.S. Geological Survey, 430 National Center, Reston, Virginia 20192.

Acknowledgments

The authors are grateful to Chris Ellis and Martin Wosnik, St. Anthony Falls Laboratory, University of Minnesota, for assistance with data acquisition, experimental setup, and particle-image velocimetry measurements. We would also like to thank Bernard Boudreau, Chris Rehmman, and one unknown reviewer for their helpful comments in preparing this manuscript.

This work was supported by the National Center for Earth-surface Dynamics (NCED), a Science and Technology Center funded by the Office of Integrative Activities of the National Science Foundation under agreement EAR-0120914. The open channel experiment used data from StreamLab, a collaborative experimental program of NCED.

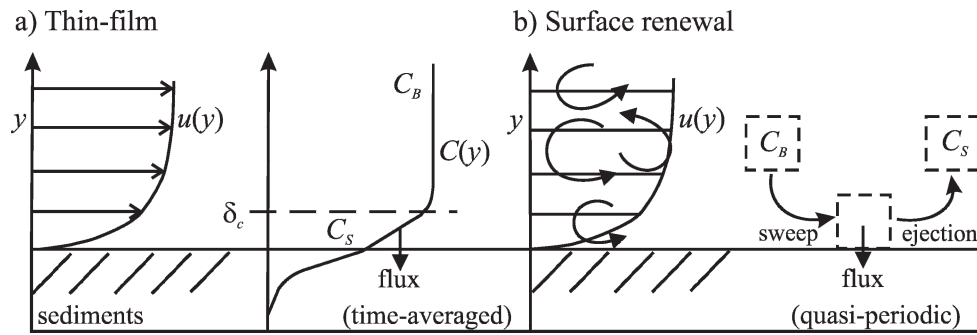


Fig. 1. Diagram of the (a) thin-film and (b) surface-renewal theories for DO flux at the sediment–water interface.

direction) that was periodically renewed by large eddies moving along the surface of the sediments (Fig. 1).

Coherent structures in turbulent flows are a fundamental yet largely unresolved topic of turbulence research. A rigorous examination of coherent structures is beyond the scope of this study (e.g., Robinson 1991; Nezu and Nakagawa 1993). In general, coherent structures are formed by streamwise-oriented vortices that begin along the sediment surface, grow, and eventually lift away into the bulk flow. This cyclic process of sweep and ejection motion is referred to as a bursting event (Robinson 1991). Bursting events create large velocity fluctuations near the sediments and also generate a self-sustaining mechanism of turbulence production for the entire flow field (Nezu and Nakagawa 1993). In chemical engineering systems (Dworak and Wendt 1977; Campbell and Hanratty 1983) and in the atmospheric boundary layer (Katul et al. 1997), these sweep and ejection motions, associated with coherent structures, have been shown to be important for quantifying momentum, mass, and heat fluxes to surfaces and to create a physical mechanism for particle entrainment in mobile sediment beds (García et al. 1996).

Observations of temporal fluctuations of the microscale DO concentration profiles suggest that diffusion across a steady-state DSL may not be the dominant transport mechanism, and the role of coherent motions should be incorporated into modeling DO transfer to sediments. In this study, we examined the role of quasi-periodic coherent motions in the flow on DO transfer to sediments using microscale DO concentration measurements and high-resolution fluid-flow characterization under channel and open-channel flow conditions. The sweep and eject motions observed within the DSL were quantified using both DO concentration fluctuations and fluid-flow measurements near the sediment–water interface. The average time between bursting events was incorporated into a semi-analytical similarity model—closely related to the surface-renewal theory and the Pinczewski and Sideman (1974) model—to describe DO flux in terms of quasi-periodic coherent motions within the DSL. The similarity model results were compared to experimental estimates of the dimensionless mass transfer coefficient derived using the surface-renewal and thin-film theories for quantifying DO transfer to sediments.

Background information

DO transfer to sediments is controlled by fluid-flow conditions and the concentration gradient from the bulk fluid to the sediments. The overall flux can be described by the integrated form of Fick's Law

$$J = k(C_B - C_s) \quad (1)$$

where J is the DO flux to the sediments, k is the mass transfer coefficient, C_B is the bulk water DO concentration, and C_s is the DO concentration at the sediment–water interface. For the thin-film theory, k is expressed as

$$k = \left(\frac{D}{\delta_c} \right) \quad (2)$$

where D is the molecular diffusion coefficient, and δ_c is the DSL thickness. Mass transfer according to the surface-renewal theory is associated with parcels of fluid periodically being transported from the bulk fluid to the sediment surface, and k is expressed as

$$k = \sqrt{\frac{D}{\tau}} \quad (3)$$

where τ is the average residence time of the parcels of water traveling along the sediments.

Thin-film theory has been applied by researchers to calculate flux in aquatic systems using an estimation of δ_c based on a concentration profile and fluid-flow characteristics. There are several methods available for estimating δ_c that produce variable results, and small changes in δ_c can greatly impact the calculated flux. One of the first methods developed to estimate δ_c (referred to as the bulk method, δ_{CB}) extrapolated the linear DO concentration profile from the sediment–water interface until it intersected the bulk DO concentration (Jørgensen and Revsbech 1985). Other researchers have defined the DSL thickness by the linear portion of the DO concentration profile only (linear method, δ_{CL}) as inferred using Fick's first law for diffusion (e.g., Røy et al. 2004). A more objective method was developed by Hondzo (1998), where δ_c was defined by the gradient of the similarity group $(C - C_s)/(C_B - C_s)$ (similarity method, δ_{CS}). More recent studies have included the effects of turbulent diffusion where the DO concentration profile is described

using an analytically derived power law (power law, δ_{CP} ; Hondzo et al. 2005) or an empirically based hyperbolic tangent function (Nishihara and Ackerman 2007).

The surface-renewal theory has been used in chemical engineering investigations examining the mass transfer of ionic solutions to a solid boundary for flows with large Reynolds numbers, Re , where $Re > 10^4$ (Dworak and Wendt 1977; Campbell and Hanratty 1983). These studies have shown that fluid-flow within a thin layer next to the wall (thickness $y^+ = yu^*/\nu = 1$) controls mass transfer. This wall layer gets renewed periodically by sweep and eject motions, and the mean period between bursting events scales with wall variables (shear stress velocity, u^* , and kinematic viscosity, ν) according to

$$T = a_1 \frac{\nu}{u_*^2} \quad (4)$$

where T is the average period between bursting events and a_1 is a dimensionless scaling constant (~ 200 – 300 , Pinczewski and Sideman 1974).

The control of DO transfer to the sediment–water interface is a function of the momentum flux and diffusion properties of the fluid. In dimensionless form, this can be described using a Sherwood (Sh), Reynolds (Re), and Schmidt (Sc) number relationship expressed by

$$Sh = f(Re, Sc) = \frac{kL}{D} = f\left(\frac{UL}{\nu}, \frac{\nu}{D}\right) \quad (5)$$

where L is the characteristic length scale for the flow geometry and U is the average velocity. Empirical evidence has shown that k scales with u^* and Sh scales as Re^{-1} (Shaw and Hanratty 1977; Steinberger and Hondzo 1999; Boudreau 2001). Scaling arguments based on small-scale eddies show that Sh scales as $Sc^{1/3}$, while the presence of large-scale eddies, with characteristic sizes relative to the flow domain, show that Sh scales as $Sc^{1/2}$ (Hondzo 1998). Development of a robust Sh – Re – Sc relationship is desirable for describing mass transfer in a fluid system because it allows for calculation of the overall flux according to Eq. 1 with the only required information being that of the fluid-flow characteristics and a measurement of the concentration gradient relevant to the mass flux across the sediment–water interface.

Similarity model

This section presents a semi-analytical, similarity model for quantifying the dimensionless mass transfer coefficient (Sherwood number, Sh), using the conceptual model of surface renewal. Introduction of similarity to the governing equations provides an alternative, less complex, derivation of a Sh – Re – Sc relationship than the Pinczewski and Sideman (1974) model. As a sweeping eddy delivers a parcel of water to the sediment surface, as shown in Fig. 1b, the steady-state DO flux across the sediment–water interface can be described by the advection-diffusion equation

$$u \frac{\partial C}{\partial x} = D \frac{\partial^2 C}{\partial y^2} \quad (6)$$

This second-order partial differential equation can be simplified to an ordinary differential equation by introducing two grouping variables: (1) the dimensionless DO concentration

$$\tilde{C} = \frac{C - C_s}{C_B - C_s} \quad (7)$$

where \tilde{C} is the DO concentration at a height y above the sediments, and (2) the similarity group

$$\eta = y \left(\frac{u_*^2}{\nu D x} \right)^{1/3} \quad (8)$$

Substituting these variables into Eq. 6 and using the near-wall velocity approximation

$$u = \frac{u_*^2 y}{\nu} \quad (9)$$

results in the governing transport equation

$$\frac{d^2 \tilde{C}}{d\eta^2} + \frac{\eta^2 d\tilde{C}}{3 d\eta} = 0 \quad (10)$$

with boundary conditions $\tilde{C} = 0$ at $\eta = 0$ and $\tilde{C} = 1$ at $\eta = \infty$ (a distance far from the sediment–water interface in the bulk flow). Equation 10 can be integrated twice and solved in terms of \tilde{C} using the boundary conditions listed above to yield

$$\tilde{C} = 1 - \frac{\int_0^\eta e^{-\frac{\eta^3}{9}} d\eta}{\int_0^\infty e^{-\frac{\eta^3}{9}} d\eta} \quad (11)$$

which can be simplified using the gamma function presented in Probstein (1989) to yield

$$\tilde{C} = 1 - 0.538 \int_0^\eta e^{-\frac{\eta^3}{9}} d\eta \quad (12)$$

Equation 12 represents a dimensionless expression that describes the DO concentration profile along the developing boundary layer occurring as a parcel of water sweeps along the sediment–water interface. The DO flux to the sediments, by definition, is related to the concentration gradient at the sediment–water interface by

$$J = -D \left(\frac{\partial C}{\partial y} \right) \Big|_{y=0} \quad (13)$$

Rewriting Eq. 12 in terms of C by substituting back in the similarity grouping variables in Eqs. 7 and 8 and differentiating with respect to y at the sediment–water interface results in the expression

$$J = 0.538 D (C_B - C_s) \left(\frac{u_*^2}{\nu D x} \right)^{1/3} \quad (14)$$

Setting Eq. 14 equal to Eq. 1 and solving for k gives an equation for the local mass transfer coefficient as a function of its position in the streamwise direction of the sweeping

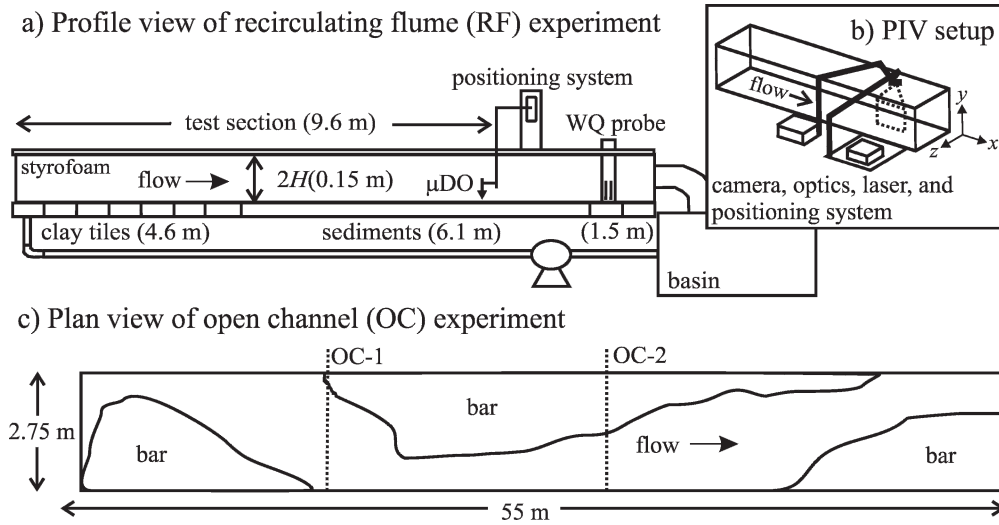


Fig. 2. (a) Diagram of laboratory RF, (b) PIV setup, and (c) OC experiments.

parcel of water expressed by

$$k(x) = 0.538 \left(\frac{D^2 u_*^2}{\nu x} \right)^{1/3} \quad (15)$$

In order to estimate an average mass transfer coefficient, the average length over which eddies sweep along the interface is estimated as

$$x_L = T u_s \quad (16)$$

where T is the average time that a parcel of water spends along the interface according to Eq. 4, and $u_s = u_*/2$ is the average velocity above the sediments calculated as a depth average of Eq. 9 to a height of $y^+ = 1$. Integrating Eq. 15 from 0 to x_L gives the average mass transfer coefficient equation

$$k_{avg} = 0.807 \left(\frac{D^2 u_*^2}{\nu x_L} \right)^{1/3} \quad (17)$$

Rewriting x_L in terms of u_* , ν , and a_1 according to Eq. 16 and regrouping terms results in the expression

$$k_{avg} = \frac{0.807}{\left(\frac{a_1}{2}\right)^{1/3}} u_* Sc^{-2/3} \quad (18)$$

which can be used in Eq. 1 to quantify the DO flux to sediments, assuming the dominant transport mechanism is sweep-and-ejection motion. Equation 18 can be made dimensionless into a $Sh-Re-Sc$ relationship by multiplying both sides by L/D , and rewriting u_* in terms of the friction factor according to

$$\frac{C_f}{2} = \frac{u_*^2}{U^2} \quad (19)$$

where the characteristic length scale is the channel half-depth, H , for recirculating flume (RF) experiments and the hydraulic radius, R , for open channel (OC) experiments.

The resulting expression describes the dimensionless mass transfer coefficient as

$$Sh = \frac{0.807}{\left(\frac{a_1}{2}\right)^{1/3}} \sqrt{\frac{C_f}{2}} Re Sc^{1/3} \quad (20)$$

with the only parameterizations being the average time that a parcel of water spends along the sediment–water interface (Eq. 4) and C_f . The derived similarity model expresses Sh as proportional to $Sc^{1/3}$ independent of the scaling arguments used in the work by Hondzo (1998).

Experimental methods

Experiments were conducted in a recirculating flume (RF experiments) and a flow-through open channel (OC experiments) both located at St. Anthony Falls Laboratory (University of Minnesota, Minneapolis). The different experimental setups provided varying fluid-flow velocities and flow geometries for studying DO transfer to sediments (Fig. 2). Sweep and ejection motions in the flow were examined using particle-image velocimetry (PIV) for RF experiments and acoustic-Doppler velocimetry (ADV) in OC experiments. DO concentrations were measured using oxygen microsensors described below. This section describes the RF and OC experimental setups individually.

RF experiments—The recirculating flume was 12.19-m long and 0.15-m wide, with a water depth ($2H$) of 0.15 m and side walls made of glass (Fig. 2a). The basin on the downstream end of the flume held a volume of 0.53 m³ and water was recirculated by a 2.2 kW centrifugal pump (Teel). A series of flow straighteners were located at the inlet of the flume to reduce turbulence at the entrance. Clay tiles lined the first 4.57 m of the flume length for flow development and the last 1.52 m to maintain exit conditions. Atmospheric reaeration at the water surface was prevented by suspending styrofoam sections over the flume and the basin, which also produced channel-flow condi-

Table 1. Flow and turbulence characteristics for RF and OC experiments.

Exp.	U_1 (cm s ⁻¹)	u_* (cm s ⁻¹)	Re	ϵ (10 ⁻⁶ m ² s ⁻³)	η_k (mm)	η_B (mm)
RF-1	3.50	0.19	2,950	1.2	0.88	0.05
RF-2	5.25	0.25	4,425	3.7	0.65	0.04
RF-3	7.50	0.34	6,320	7.5	0.51	0.03
RF-4	9.50	0.43	8,005	13.7	0.40	0.03
RF-5	11.00	0.50	9,270	16.4	0.36	0.03
OC-1	1.00	0.15	900	—	—	—
OC-2	5.00	0.41	8,990	60.7	0.33	0.02

U_1 = free-stream velocity; u_* = shear stress velocity; Re = Reynolds number; ϵ = energy dissipation rate; η_k = Kolmogorov scale; and η_B = Batchelor scale.

tions (characteristic length scale, $L = H$) with an aspect ratio of 1:1. Deionized water was used for all RF experiments.

Synthetic sediments were used that consisted of sand (81% of dry weight), clay (15%), peat moss (2%, sieved to <1 mm), organic compost (1.95%, sieved to <1 mm), dolomite (0.04%), and humic acid (0.01%) according to the procedures described by Walsh et al. (1992). The sediment components were mixed dry and wetted with a mixture of deionized water, leaf leachate, and a mixed-bacterial culture (generated from natural stream sediments) to bring the final organic content of the sediment to ~10% based on loss on ignition. Sediments were placed at a depth of 2.5 cm over a length of 6.10 m in the flume and the surface of the sediments was leveled using a scraper attached to a fixed-elevation trolley above the flume. This resulted in a smooth bed of sediments with an approximate roughness height of 0.1 mm.

Fluid-flow conditions were controlled by gate valves on the recirculation line and on the outlet of the flume. At the start of each experiment, an acoustic-Doppler velocimeter (ADV, Sontek YSI) was used to monitor velocity profiles at the test-section location (9.6 m from the flume inlet). The gate valves were adjusted to maintain a constant flow depth of $2H$ and free-stream velocity (U_1 , measured at a height, H , above the sediments) ranging from 3.5 cm s⁻¹ to 11.0 cm s⁻¹ (Table 1).

Separate experiments were conducted for DO flux and fluid-flow characterization by PIV to avoid interference between measurements and flume configuration. DO flux experiments were conducted under varying water temperatures (25–37°C, Table 2) caused by seasonal temperature changes within the laboratory facility. Fluid-flow experi-

ments at the different flow rates were conducted within 1 d, and water temperatures were 25°C for all experiments.

DO measurements (RF)—A Hydrolab Datasonde 4a water quality probe (Hach) was positioned downstream of the sediment test section in the flume, and it measured bulk DO concentrations, pH, temperature, and specific conductivity every 30 min. Microscale DO concentration measurements were made using an OX-10 microsensor (Unisense). This Clark-type oxygen sensor had a tip diameter of 10 μ m and contained an internal reference and guard cathode. The DO microsensor was connected to a high-sensitivity PA2000 picoammeter (Unisense) for signal amplification. A BiSlide[®] actuator (Velmex) and VXM stepping motor controller (Velmex) were used to control the vertical and streamwise position of the DO microsensor within the flume with a spatial resolution of 4 μ m. The positioning system was located 9.6 m from the inlet of the flume (Fig. 2a), which was far enough downstream to ensure fully developed fluid-flow conditions, and could sample a streamwise span of 0.5 m and the entire flow depth including sediments in the vertical direction.

The response time of the OX-10 microsensors was tested by rapidly traversing across the concentration gradient occurring within the DSL while monitoring the recovery of the DO concentration. At an average velocity of 3.5 cm s⁻¹, a step change between 1 mg L⁻¹ and 4 mg L⁻¹ in DO concentration was achieved over a vertical distance ~1 mm. The 90% response time for a rapid change in DO concentration ranged between 0.4 s and 1.2 s for the microsensors used in this study.

DO profiles were made vertically across the sediment–water interface starting in the sediments, moving up

Table 2. Comparison of estimation methods for the diffusive sublayer thickness, δ_c , used in thin-film theory.

Exp.	T (°C)	D (10 ⁻⁵ cm ² s ⁻¹)	ν (10 ⁻² cm ² s ⁻¹)	δ_{CB} (mm)	δ_{CS} (mm)	δ_{CL} (mm)	δ_{CP} (mm)	$2\pi\eta_B$ (mm)
RF-1	25	2.40	0.89	2.21	2.26	0.68	0.59	0.29
RF-2	26	2.46	0.88	0.77	0.69	0.50	0.46	0.22
RF-3	30	2.75	0.80	0.40	0.30	0.27	0.31	0.19
RF-4	35	3.21	0.70	0.17	0.20	0.16	—	0.17
RF-5	37	3.45	0.65	0.13	0.15	0.08	—	0.16
OC-1	25	2.40	0.89	3.00	2.70	1.00	1.15	—
OC-2	25	2.40	0.89	0.40	0.60	0.25	—	0.11

T = temperature; D = molecular diffusion coefficient; ν = kinematic viscosity; δ_{CB} = bulk method; δ_{CS} = similarity method δ_{CL} = linear method; δ_{CP} = power law method; and $2\pi\eta_B$ = Batchelor scale method.

through the water column and then back into the sediments. The vertical steps ranged between 25 μm and 1 mm increments, with more measurements near the sediments. The location of the sediment–water interface was first determined by visual inspection with the aid of a magnifying glass and was later adjusted from the DO concentration profile using the slope discontinuity caused by the change in the diffusion coefficient between the water and the sediments as described by Røy et al. (2004). DO concentrations at each step were measured at a frequency of 10 Hz for a duration ranging between 2 min and 5 min. The DO concentration signal was processed using a Butterworth low-pass filter with a cutoff frequency of 1 Hz in order to eliminate electronic noise and response-time aliasing. Several DO concentration profiles were made during the course of each experiment and the DO profiles reached steady-state conditions rapidly ($\sim 1\text{--}2$ d).

Fluid-flow characterization (RF)—PIV experiments were conducted under the same range of flow conditions as the DO flux measurements by matching sediment texture, ADV profiles, water depth ($2H$), and discharge prior to start. They also were carried out at a streamwise distance of 9.6 m from the inlet to allow for fully developed flow conditions. PIV measurements provided instantaneous velocity measurements over a 2D plane (field of view, 45×45 mm) in the flow direction by calculating particle displacements from illuminated particle-image pairs.

The PIV measurements were made using a Ultra PIV system (TSI Instruments). The laser light sheet was generated in the x – y plane (Fig. 2b) by a dual-pulsed Nd:YAG (Neodymium:Yttrium Aluminum Garnet) laser passed through 25-mm cylindrical and 50-mm spherical lenses, positioned with an optical light-arm connected with the laser on an optical breadboard. Images were recorded using a POWERVIEW™ (2048 \times 2048 pixels, 12-bit, with frame-straddling capability) CCD camera with a 105-mm focal-length lens and Scheimpflug mount, along with a frame grabber and a desktop computer. The camera was mounted on the Velmex positioning system, described previously, which was also connected to the cylindrical and spherical lenses attached to the optical light-arm (Fig. 2b). This configuration allowed for proper alignment of the optics and positioning of the field of view directly along the sediment–water interface. Timing of the laser and camera was controlled using a synchronizer, which captured particle-image pairs at a rate of approximately 1 Hz (a total of 800 particle-pair images was captured for each experiment). The entire PIV system was programmed using INSIGHT™ 5.5 software (TSI Instruments).

The water was seeded with neutrally buoyant, hollow glass spheres with an average diameter of 14 μm (3 pixels on image), and the seeding concentration was adjusted to give ~ 10 particles per interrogation window. The particle-image pairs were processed using a 32×32 pixel interrogation window with a 50% overlap. Velocity vectors were computed using a cross-correlation between particle-image pairs using a recursive Nyquist grid, Hart correlation engine, and a bilinear peak-finding algorithm. The resulting 127×127 vector field had a calibration factor of

21.978 $\mu\text{m pixel}^{-1}$ and a minimum spot-size resolution of 0.7 mm. Particle displacement errors caused by bias in the cross-correlation procedure were ~ 0.1 pixels for a 32×32 pixel interrogation window and similar seeding and optical conditions according to the work by Westerweel (1997). An average particle displacement of 10 pixels between particle-pair images resulted in an error in the velocity vectors of approximately 1% in the streamwise direction and 10% in the vertical direction.

OC experiments—OC experiments were conducted in a flume 55 m in length and 2.75 m wide (Fig. 2c). The experimental channel drew in Mississippi River water from the upstream pool of St. Anthony Falls (Minneapolis, Minnesota), and the discharge was controlled by a mechanical gate at the upstream intake. The water depth for the open channel was controlled by a weir located at the downstream end of the channel. Sediments were added to the channel to create a depth of 70 cm. The sediments consisted of a mixture of sand- (<2 mm) to gravel- ($D_{50} = 9$ mm) sized particles (resulting mixture $D_{50} \sim 5$ mm). The bed geomorphology (Fig. 2c) was formed at a discharge of 320 L s^{-1} and a flow depth of 15 cm with sediment recirculation, which was sustained until an equilibrium pattern of alternating bars was established. The resulting bed slope was $\sim 1\%$.

The discharge was lowered to 15 L s^{-1} and the water depth varied from 5 cm to 20 cm for the DO flux experiments. With the lower discharge, fine benthic organic material settled onto the bed surface creating a floc layer ~ 1 mm thick over most of the channel. There were two test cross-sections for DO and ADV measurements: a low velocity section located at 17 m (OC-1 Fig. 2c, $U_1 = 1 \text{ cm s}^{-1}$) and a high velocity section located 26 m downstream (OC-2 Fig. 2c, $U_1 = 5 \text{ cm s}^{-1}$). The corresponding hydraulic radii ($R = A/P_w$, where R was the characteristic length scale for OC flow, A was the cross sectional area, and P_w was the wetted perimeter) were 8.0 cm and 7.4 cm for the low- and high-velocity cross-sections, respectively. Water temperatures were constant at 25°C for the duration of the experiment, and DO concentration profiles and ADV measurements were performed on the same day because simultaneous measurements were not possible.

DO measurements (OC)—DO concentration profiles were made using an OX-N needle sensor (Unisense). This Clark-type oxygen sensor had a tip diameter of 1.1 mm and contained an internal reference and guard cathode. The sensor was encased in a 55-mm-long needle for protection from the larger sediment particles of the OC experiment. The DO signal was channeled to an amplifier and processed with a low-pass filter as described previously. The DO needle sensor was positioned in the open channel using a point gage (Rickly Hydrological) with 1-mm precision, which was attached to a structural aluminum bridge attached to the side walls of the channel.

Profiles were made starting within the water column and traversing into the sediments. The steps ranged between 0.5-mm and 2-mm increments, with closer spacing near the sediments. The sediment–water interface was initially determined from measurements of the point gage from

the fixed elevation of the structural aluminum bridge and was modified using the slope discontinuity in the DO concentration profile discussed previously. The DO needle sensor was sampled at a rate of 1 Hz for 2 min to 5 min at each vertical location in the profile. The disturbance of the OX-N needle tip on the boundary layer was assessed using the method described by Hondzo et al. (2005). The local Re value was estimated as $Re = ud/v = 15$, where d was the needle-tip diameter and u was the velocity at the top of the DSL at the high-velocity section in the OC experiment (OC-2, Table 1). This local Re value corresponded to unseparated flow at the sensor tip, so the effect of the needle tip on the boundary layer was minimal.

Fluid-flow characterization (OC)—ADV measurements were made near the sediments using a 16-MHz MicroADV (Sontek YSI) with a sampling volume of 0.1 cm³. The ADV was positioned in the test cross-sections using a mechanical traversing system attached to the structural aluminum bridge. A 10-min recording of the 3D flow field was sampled at 50 Hz at each location. ADV data was filtered using WinADV (U.S. Bureau of Reclamation) software for average signal correlations >70%, signal-to-noise ratios >10 dB, along with the phase-space threshold de-spiking algorithm.

Quantification of bursting events and turbulence characteristics

Bursting events were identified using velocity and DO concentration data independently through the detection of ejection motions near the sediments. For velocity data (PIV for RF and ADV for OC experiments), ejections were identified as quadrant II (Q_2) events. The fluctuating velocity components in the streamwise (x) and vertical (y) direction, u' and v' respectively, could be used to categorize ejection motions by quadrant location in plot of v' versus u' . Ejection motions (Q_2 events) occurred in the upper-left corner of the plot with $v' > 0$ and $u' < 0$. For DO concentration data, ejection motions were identified as large, negative oscillations representing the ejection of a low DO concentration parcel of water (Fig. 1b).

As coherent structures sweep along the sediments and lift upward into the main flow, they can generate multiple ejections associated with this single bursting event. The similarity model described previously required the average time between bursting events, so the burst detection algorithms described below also had to account for multiple ejections associated with a single bursting event. This was done by estimating the maximum time between ejections, τ_{\max} , as described by Bogard and Tiederman (1986). Ejections separated by a time less than τ_{\max} were grouped into a single burst. We used a different method for approximating τ_{\max} than described by Bogard and Tiederman (1986) because we used PIV, ADV, and DO concentration data for the detection of ejections, which all have different sampling frequencies. Instead, τ_{\max} was estimated as an advective timescale of a typical coherent structure near the sediment-water interface assuming a streamwise length scale of $x^+ = xu^*/v = 200$ (typically $x^+ = 100$ –500, e.g., García et al. 1996) and a velocity scale according to Eq. 9.

Burst detection from velocity data—For each RF experiment, 800 PIV vector fields sampled over a period of ~15 min were used to calculate an average velocity map of the streamwise and vertical velocity and root-mean-square components (u , v , u_{rms} , v_{rms}). The average velocity map was subtracted from individual PIV vector fields to produce maps of the fluctuating velocity components, u' and v' . An algorithm was used to sequentially examine each PIV vector field and produce a depth profile of the fluctuating velocities by averaging values along the streamwise direction. The Q_2 events were identified using the criteria $u' < 0$, $v' > 0$, and $u'v' > \Phi\sigma_{u'}\sigma_{v'}$, where $\sigma_{u'}$ and $\sigma_{v'}$ were the streamwise averaged root-mean-square velocities, and Φ was referred to as the hole size, which was set equal to one according to the work of Bogard and Tiederman (1986). The time stamp for individual PIV vector fields with Q_2 events was recorded, and the period between individual bursting events was calculated by difference. The detection of Q_2 events was performed at a height of $y^+ = 15 \pm 4$ (± 4 relates to the PIV measurement resolution, or spot size) to be consistent with previous studies. Within this region of the flow ($y^+ < 20$), turbulence production, dissipation, and kinetic energy all had peak values, which related to the presence of coherent motions (Pope 2000).

For the OC experiment, an ADV was used to measure the u , v , and w (spanwise) velocity components at a frequency of 50 Hz. The ADV's sampling volume was positioned as close to the sediment-water interface as possible, which resulted in $y = 7.5$ mm ($y^+ = 13$) at the low-velocity section and $y = 4.0$ mm ($y^+ = 18$) at the high-velocity section. Q_2 events were detected in the manner described previously for PIV data.

Burst detection from DO concentration data—The DO concentration time series corresponding to a dimensionless height of $y^+ = 1$ was used to detect bursting events for each experiment with varying fluid-flow conditions. For each time series, the mean DO concentration was subtracted out leaving the fluctuating concentration component, C' . Ejections were detected using the criteria $C' < 0$ and $|C'| > \sigma_{C'}$, where $\sigma_{C'}$ was the standard deviation of C' .

Fluid-flow and turbulence characteristics—PIV data was used to calculate mean flow and turbulence characteristics relevant to mass transfer at the sediment-water interface for RF experiments (Table 1). The slope of the logarithmic velocity profile was used to calculate u_* for the flow conditions of each experiment using time-averaged vector fields. The energy dissipation rate, ε , was estimated from velocity gradients using the direct measurement expression proposed by Luznik et al. (2007):

$$\varepsilon = 4v \left\langle \left(\frac{\partial u}{\partial x} \right)^2 + \left(\frac{\partial v}{\partial y} \right)^2 + \frac{3}{4} \left(\frac{\partial u}{\partial y} \right)^2 + \frac{3}{4} \left(\frac{\partial v}{\partial x} \right)^2 + \frac{\partial u}{\partial x} \frac{\partial v}{\partial y} + \frac{3}{2} \left(\frac{\partial u}{\partial y} \frac{\partial v}{\partial x} \right) \right\rangle \quad (21)$$

where $\langle \rangle$ denoted time ensemble and ε was spatially-

averaged between $y^+ = 20$ to $y^+ = 100$ to capture the logarithmic region of the flow.

ADV data was used to calculate mean flow and turbulence characteristics for OC experiments (Table 1). The time average of the Reynolds stress ($u'v'$) was used to calculate u_* from the linear $u'v'$ profile that was a characteristic of uniform flows. Measurements of the velocity gradients were not available with ADV data, so ε was estimated using the expression for homogeneous isotropic turbulence including Taylor's "frozen-flow" hypothesis to allow for the use of time series ADV data according to

$$\varepsilon = \frac{15\nu}{u^2} \left(\frac{\partial u'}{\partial t} \right)^2 \quad (22)$$

Similar estimates of ε were obtained using the log-law estimation, $\varepsilon = u_*^3/\kappa y$, where κ was the von Kármán constant taken to be 0.4.

The Kolmogorov (η_K) and Batchelor scales (η_B) were calculated using $\eta_K = (\nu^3/\varepsilon)^{1/4}$ and $\eta_B = (\nu D^2/\varepsilon)^{1/4}$, respectively. The PIV spot-size resolution of 0.7 mm was similar to the estimated η_K values. The sampling frequency of ADV was 50 Hz, or 0.02 s, much less than the Kolmogorov timescale, $t_K = (\nu/\varepsilon)^{1/2}$, which was ~ 0.1 s for experiment OC-2 (Table 1). Both of these results indicate that PIV and ADV measurements were capable of resolving the scales of the motions responsible for the majority of the dissipation in the flow (Pope 2000). The Batchelor scale was used to estimate the DSL thickness using, $\delta_c = 2\pi\eta_B$, according to the work by Lazier and Mann (1989), with results listed in Table 2.

Results

DO concentration profiles and δ_c estimates—Time-averaged DO concentration profiles show decreasing DSL thickness with increasing Re as the DO gradient layer was compressed towards the sediment–water interface (Fig. 3). DO concentration profiles penetrated into the sediment to a depth of ~ 1 mm in RF experiments and to a depth of 3 mm in OC experiments. The DO concentration at the sediment–water interface increased with increasing Re from $C_s/C_B = 0.4$ for $Re = 2,950$ to $C_s/C_B = 0.9$ for $Re = 9,270$.

The various methods used to quantify the thickness of the DSL, δ_c , are shown in Table 2. The bulk and similarity methods (δ_{CB} and δ_{CS}) produced similar results that, with few exceptions, were larger than those from the other methods. The linear and power-law methods produced similar values of the DSL thickness; however, δ_c for larger Re values (experiments RF-4, RF-5, and OC-2, $Re = 8,005$, 9,270, and 8,990, respectively) was difficult to estimate because the concentration gradient occurred over a distance of ~ 0.1 mm. Of estimates made using the linear method for the profiles in experiments RF-4 and RF-5, only two to three data points were located within the DSL. The small DO concentration difference between the bulk and at the sediment–water interface, along with difficulty in estimating the turbulent diffusion coefficient near the sediments, did not allow for calculation of δ_{CP} for the fluid-flow conditions of experiments RF-4, RF-5, and OC-2. The

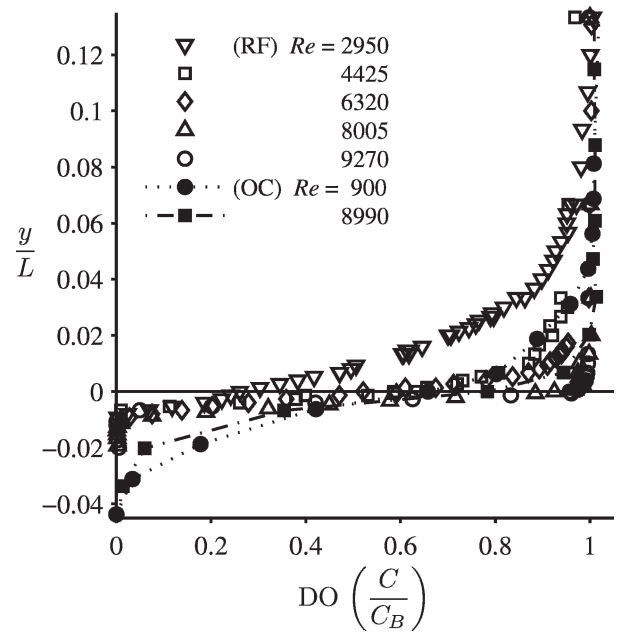


Fig. 3. Time-averaged DO concentration profiles under varying fluid-flow conditions. The y -axis is normalized by the characteristic length scale of the flow, L (equal to the flume half-depth, $H = 0.075$ m, for RF experiments and the hydraulic radius, $R = 0.080$ and 0.074 m, in OC-1 and OC-2 experiments, respectively).

Batchelor scale estimates ($2\pi\eta_B$) of the DSL thickness produced the smallest range in values with varying fluid-flow conditions and were lower than the other estimation methods in general.

The standard deviation of the individual DO time series used to generate the time-averaged DO concentration profiles in Fig. 3 show large deviations near the sediment–water interface (Fig. 4). The maximum deviation for each experiment occurred near the top of the DO concentration gradient (at $y^+ \sim 1$ for all experiments) shown in Figs. 3 and 4, which progressed closer to the sediments with increasing Re . The peak in the DO standard deviation profiles for the fluid-flow conditions of RF experiments RF-4, RF-5, and both OC experiments penetrated across the sediment–water interface.

Coherent motions and bursting events—Flow-visualization experiments have identified coherent motions by observing shear layers that are lifted away from the interface and are referred to as "hairpin vortices" (Robinson 1991). Shear layers correspond to thin sheets of concentrated spanwise vorticity (ω_z) expressed by

$$\omega_z = \frac{\partial v}{\partial x} - \frac{\partial u}{\partial y} \quad (23)$$

Figure 5 shows PIV images of ω_z and velocity direction and magnitude for RF experiments RF-2 ($Re = 4,425$) and RF-5 ($Re = 9,270$). Both flow conditions demonstrate shear layers with concentrated vorticity, and steep gradients in the streamwise velocity magnitude vectors above the

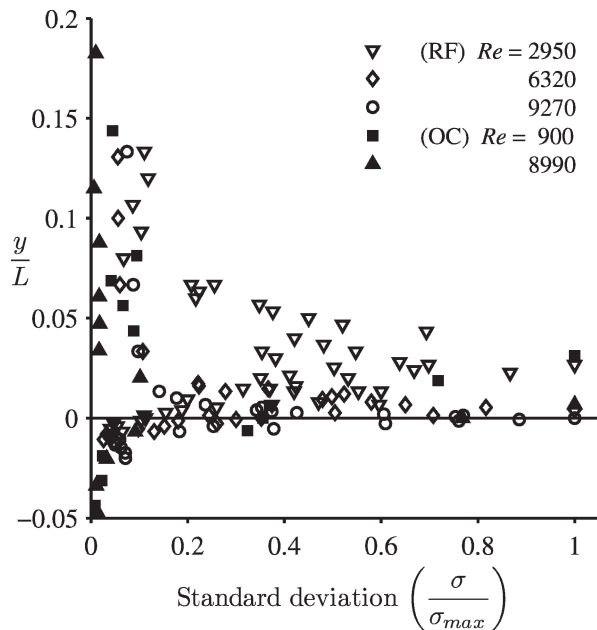


Fig. 4. Profile of the standard deviation in DO concentration time series under varying fluid-flow conditions. The y -axis is normalized by the characteristic length scale of the flow, L (equal to the flume half-depth, $H = 0.075$ m, for RF experiments and the hydraulic radius, $R = 0.080$ and 0.074 m, in OC-1 and OC-2 experiments, respectively).

sediments. These shear layers were observable for all RF experiments, including the lowest fluid-flow conditions of experiment RF-1 ($Re = 2,950$), which fell into the transitional zone between laminar and turbulent flow.

Contributions from each quadrant (Q_1 , Q_2 , Q_3 , Q_4 , Fig. 6 inset) to the Reynolds shear stress, $u'v'$, were calculated from the PIV data for experiment RF-3 ($Re = 6,320$) in Fig. 6. Ejection events, Q_2 , contributed slightly more to the Reynolds shear stress than sweep events, Q_4 , which is consistent with the results presented by Nakagawa and Hanratty (2003). This plot shows that the majority of the shear stress near the sediments was generated by Q_4 sweep and Q_2 ejection motions.

The large DO standard deviations observed near the sediment in Fig. 4 corresponded to DO concentration time series that had an undulating pattern (Fig. 7a). The characteristic timescales of these large oscillations were estimated by examining the power spectral density of the signal as shown in Fig. 7b (for experiment RF-3, $Re = 6,320$). Several peaks with high energy were observable with periods between 9 s and 30 s. At higher frequencies, the DO energy spectrum decayed with a slope of $-5/3$, which was characteristic of a passive scalar in a turbulent flow (Chapter 8.6, Tennekes and Lumley 1972). Figure 7a displays the location of the detected bursting events (according to the algorithm described previously) in the DO concentration time series with an average bursting period of 18.75 s. A weighted average of the periods associated with the large peaks in the DO energy spectrum had a timescale of 19.25 s. This agreement between the burst detection algorithm and peaks in the DO energy spectrum was observed in all experiments.

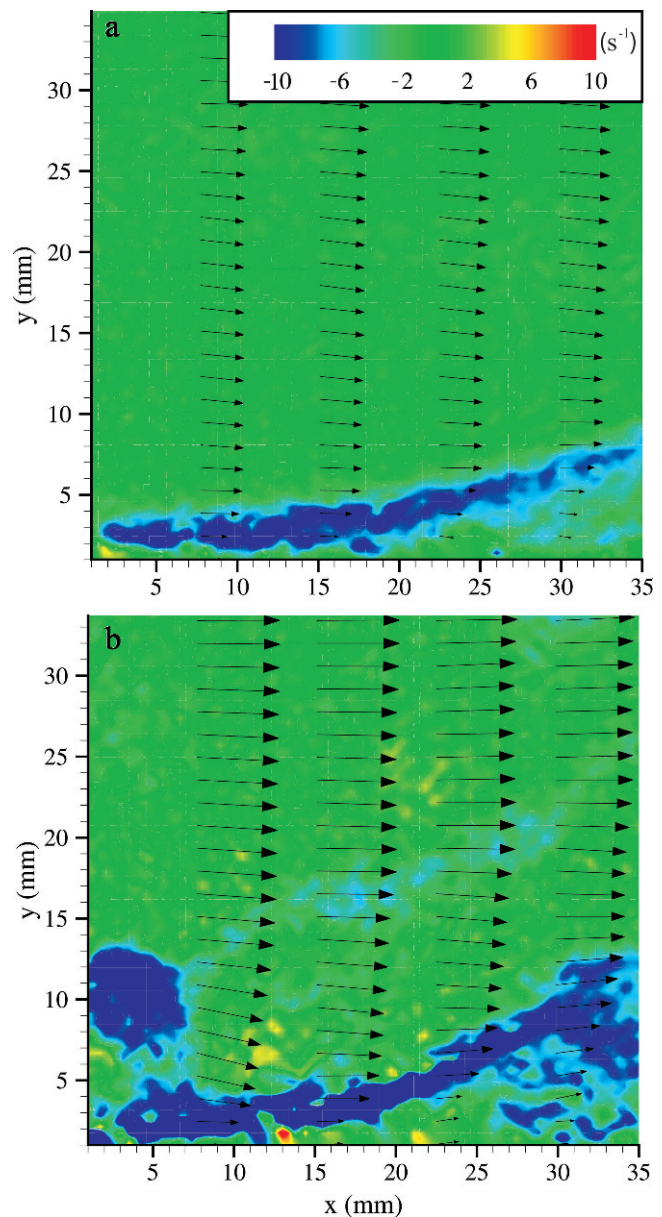


Fig. 5. PIV vorticity in the spanwise direction with velocity magnitude and direction vectors (arrows) for (a) fluid-flow conditions in experiment RF-2 ($Re = 4,425$) and (b) fluid-flow conditions in experiment RF-5 ($Re = 9,270$).

The average time between bursting events ranged between 12 s and 91 s for all experimental fluid-flow conditions. Burst detections from DO concentration data were consistent with those from velocity data as shown in Fig. 8. For smaller periods between bursting events (corresponding to higher fluid-flow velocities) the burst detections between DO concentration and velocity data were nearly identical, falling on a 1:1 line. At larger periods between bursting events (corresponding to lower fluid-flow velocities), the velocity data predicted a longer time between bursting events than the DO concentration data.

The average period between bursting events (using velocity data) plotted against the characteristic wall time-

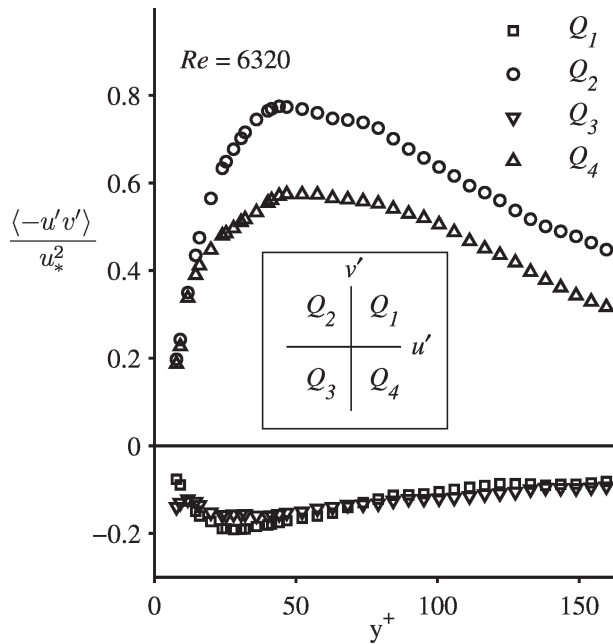


Fig. 6. Contributions from each quadrant to the Reynolds shear stress for fluid-flow conditions of experiment RF-3 ($Re = 6,320$). The quadrants Q_1 , Q_2 , Q_3 , and Q_4 are defined by the plot of the fluctuating velocity components v' versus u' as shown in the inset.

scale (v/u_*^2) is shown in Fig. 9. The experimental data supports the linear relationship ($R^2 = 0.95$, slope = 238.5) of Eq. 4. The slope of the scaling relationship between the average time between bursts and wall variables ($a_1 = 238.5$) was used to calculate Sh by the similarity model describe in Eq. 20, and fell within the expected range discussed by Pinczewski and Sideman (1974). The scaling of the average time between bursts by wall variables has been experimentally derived for flows with $Re > 10^4$, and the results of this study extend the range of Eq. 4 down to flows with $Re \sim 10^3$.

Similarity model, thin-film, and surface-renewal theories—The similarity model was calculated using a Blasius expression for the friction factor (Pinczewski and Sideman 1974)

$$\frac{C_f}{2} = 0.023Re^{-0.2} \quad (24)$$

with Sc ranging from 188 to 371 to bound the temperature range in experimental conditions (Table 1). The overall bulk DO flux in RF experiments was calculated from the decrease in bulk DO concentration over time, which is only possible for a closed system. The k value estimated from the bulk flux was independent of the DO concentration profile and was used as a benchmark for evaluating thin-film, surface renewal, and similarity models. Equations 2 and 3 were used to estimate k for experimental data according to thin-film and surface-renewal theories using molecular diffusion coefficients and δ_c values from Table 2. For the

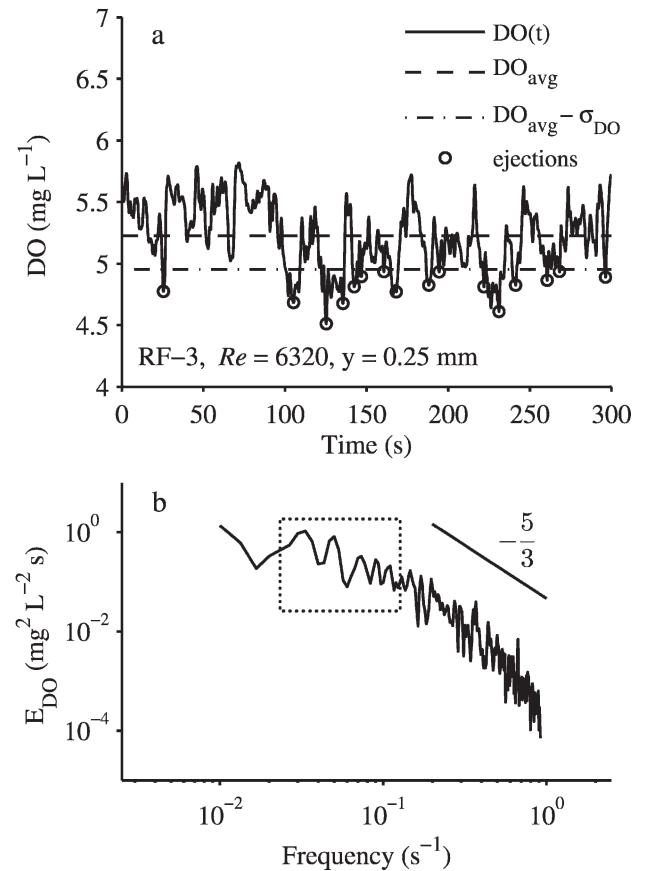


Fig. 7. (a) DO concentration time series for experiment RF-3 ($Re = 6,320$) at 0.25 mm above the sediment-water interface with burst detections shown. The average period between bursting events was 18.75 s. (b) The corresponding power spectral density of the DO concentration time series. Dotted square indicates peaks in the spectrum with corresponding periods between 9 s and 30 s and a weighted averaged of 19.25 s.

surface-renewal model, τ was set equal to the average period between bursting events according to Eq. 4.

A comparison of Sh values under varying fluid-flow conditions showed a high degree of agreement between the overall bulk flux values and the similarity model results (Fig. 10). The Sh values based on the various thin-film methods were generally lower than those of the overall bulk flux, surface renewal, and similarity models. The thin-film bulk and similarity (δ_{CB} and δ_{CS}) estimates produced the lowest Sh values of the various methods. The power-law (δ_{CP}) and linear (δ_{CL}) methods produced similar results, although the power-law method does not apply at higher Re values. For the linear method, a nonlinear dependence with respect to Re (Sh scales as Re^c , where c was a constant > 1) was observed, which contradicted the findings by Shaw and Hanratty (1977). The Sh values calculated using the Batchelor scale ($2\pi\eta_B$) and those using the surface-renewal theory produced similar results to the overall bulk flux and the similarity model, with exception for the surface-renewal theory for $Re = 900$ where the estimated Sh value was significantly larger.

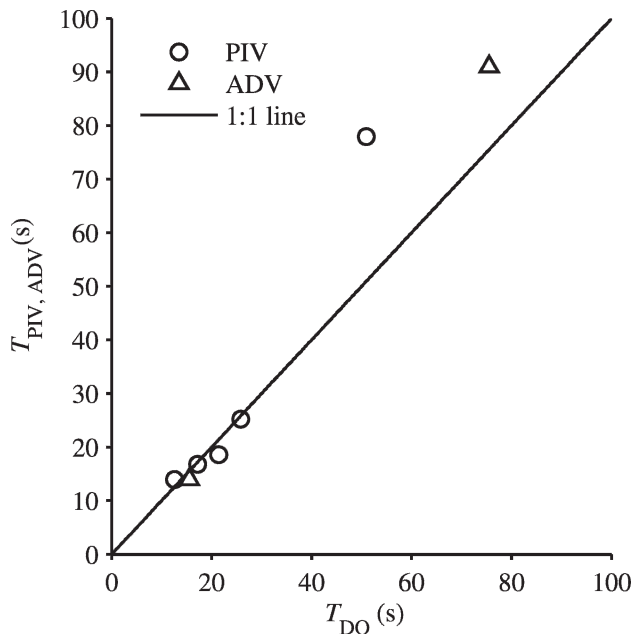


Fig. 8. Comparison of the average time between bursting events estimated using fluid-flow (PIV and ADV) measurements and DO concentration data.

Discussion

Mass flux to aquatic sediments has been traditionally calculated by thin-film theory using an estimate of δ_c from a steady-state concentration profile and fluid-flow properties. Time-averaged DO concentration profiles (Fig. 3) and estimated δ_c values (Table 2) depicted the thinness of the concentration gradient layer, and DO fluctuations (Fig. 4) near the sediments demonstrated the unsteady nature of the DSL. These two factors made estimation of δ_c difficult, which could have greatly affected the calculation of the mass transfer coefficient and flux (Fig. 10). Røy et al. (2004) demonstrated that the DSL was not a stagnant film and defined the “true” DSL as a region where DO fluctuations at different depths were in phase with each other by diffusive transport. The DO fluctuations near sediments had characteristic timescales similar to those associated with coherent motions (10 s to 100 s) rather than small-scale turbulent eddies (<1 s). Unfortunately, quantifying a “true” DSL would require measuring DO concentrations at several depths simultaneously, which is an experimental challenge.

The surface-renewal theory describes a conceptual model that is consistent with temporal DO fluctuations and transport controlled by coherent motions. The Pinczewski and Sideman (1974) model derived a $Sh-Re-Sc$ relationship using the surface-renewal theory with empirical relationships of fluid renewal to a thin layer next to the wall. This model has not been adopted by research community interested in DO mass transfer to aquatic sediments mostly due to the lack of DO concentration and fluid-flow microstructure data needed to develop the empirical relationships of renewal mass transfer to flow properties.

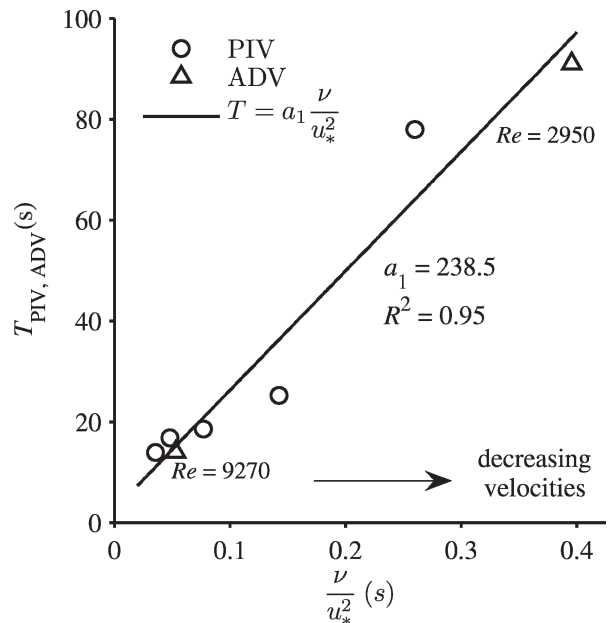


Fig. 9. Scaling of the average time between bursting events with shear stress velocity (u_*) and kinematic viscosity (ν).

PIV measurements in the RF experiments allowed for the qualitative detection of coherent motions as shear layers lifting away from the sediments (Fig. 5). Quadrant analysis of velocity fluctuations demonstrated that Q_4 sweep and Q_2 ejection motions were the largest contributors to the Reynolds shear stress near the sediments (Fig. 6). An algorithm to quantify sweep and eject motions based on Q_2 ejection motions was used with PIV and ADV measurements in RF and OC experiments, respectively. The linear relationship between the average period between bursting events and wall variables (u_* and ν) described by Eq. 4 was supported by experimental data from chemical engineering investigations (Dworak and Wendt 1977; Campbell and Hanratty 1983) and data from this study under channel and OC flow conditions (Fig. 9). The slope of Eq. 4, $a_1 = 238.5$, which was determined empirically for this investigation, was very similar to the value of 243 used in the surface-renewal model of Pinczewski and Sideman (1974). There was also a high degree of agreement between the average period between bursting events detected as Q_2 ejections in the velocity data and the characteristic timescales of the DO concentration spectrum (Figs. 7, 8), suggesting that the sweep and ejection motions were the cause for the temporal oscillations in the DO concentration data.

The similarity model described previously was also derived from the surface-renewal conceptual model of mass transfer proposed by Danckwerts (1951). The similarity grouping variables \tilde{C} and η have been presented in previous studies (Hondzo 1998; Probst 1989), and their use provided a more general $Sh-Re-Sc$ expression than derived by Pinczewski and Sideman (1974). The Sh number was quantified using the experimentally supported expression for describing bursting events (Eq. 4, Fig. 9) and an empirical relationship describing the friction factor,

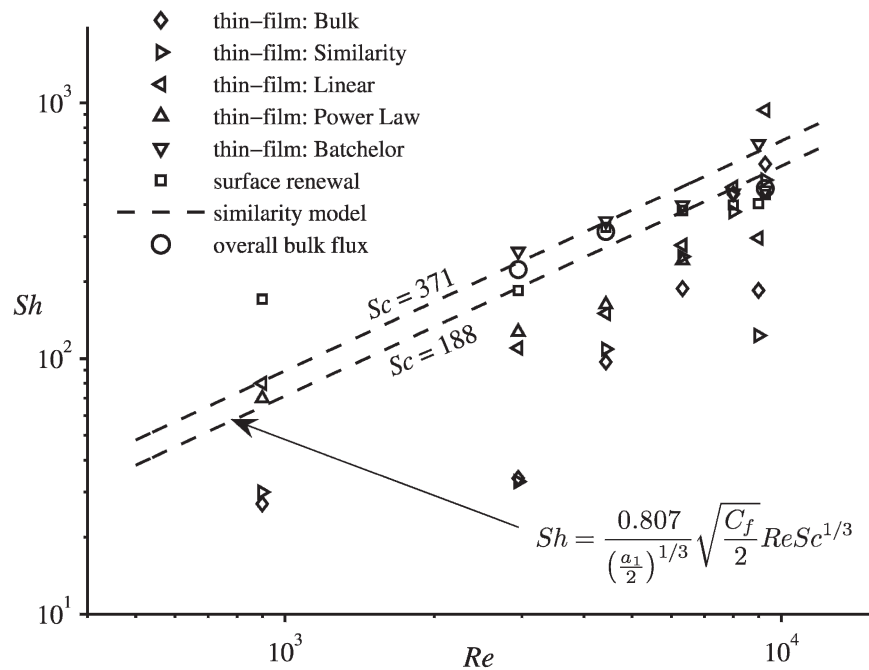


Fig. 10. Dimensionless Sherwood–Reynolds number relationship. Experimental data was used to estimate of the mass transfer coefficient (k) using thin-film and surface-renewal theories, which was made dimensionless ($Sh = kL/D$), where L is the characteristic length scale (equal to H for RF and R for OC experiments). The overall bulk flux was calculated for RF experiments as the change in bulk DO concentration over the experiment $[(dC_B/dt)(V/A_s)]$, where V is the volume of water and A_s is the surface area of the sediments.

C_f . The similarity model agreed well with experimental data of the overall bulk flux (Fig. 10). Estimations of the Sh number using thin-film theory were highly variable because of the complications in estimating δ_c and often deviated from the overall bulk flux and the similarity model results. The exception to this trend was when δ_c was estimated by the Batchelor length scale ($2\pi\eta_B$), which was a measure of fluid-flow characteristics, and thus provided further evidence that DO transfer to sediments was controlled more by the fluid-flow than diffusion across a stagnant DSL.

The surface-renewal theory depicts DO transfer to sediments by diffusion from a parcel of water within the near-wall region, which is periodically renewed by coherent motions in the flow. The governing equation for the similarity model (Eq. 6) did not include a time-dependent term, thus steady-state conditions were assumed within the renewal parcel of water, which has been proven to be a reasonable approximation by Pinczewski and Sideman (1974). Turbulent diffusion was neglected because transfer was associated with parcels of water advected to the near-wall region ($y^+ \leq 1$) where eddy viscosity decayed rapidly to zero and molecular diffusion dominated transfer (Boudreau, 2001).

Surface-renewal and thin-film theories have been examined primarily using flat surfaces. The influence of small-scale topography created by benthic fauna was found to have a small influence on DO flux calculations (Røy et al. 2002), while the presence of large-scale bedforms has been shown to enhance DO flux to sediments (Precht et al. 2004). The similarity model essentially averages the effects

of bed roughness when quantifying the mass transfer coefficient by assuming that transport is caused by sweep and ejection motions, and numerous studies on coherent structures have shown that surface roughness does not greatly affect the nature of bursting events (e.g., García et al. 1996). The effect of bedforms on DO transfer to sediments can be accounted for in the similarity model through the use of an appropriate empirical relationship describing bed roughness and shear stress distribution in aquatic systems (Keulegan or Manning–Strickler relationship). It should be noted that the surface-renewal conceptual model does not accurately represent coherent motions inherent to natural aquatic systems (Nezu and Nakagawa 1993). The complex structure of hairpin vortices, multiple ejections, and the 3D nature of coherent motions is essentially averaged into a 2D representation of sweep and ejection motions. However, empirical evidence shows that this simplified conceptual model predicts the overall bulk flux over a wide range of flow conditions including velocity, flow geometry, and bed roughness characteristics.

The challenges in quantifying DO flux to sediments are caused by the small scales over which transfer occurs and our reliance on DO microstructure measurements across the sediment–water interface. Thin-film theory has been used to interpret DO concentration profile data using a variety of empirically-derived Sh – Re – Sc relationships (Boudreau 2001). However, the accuracy of these Sh – Re – Sc relationships in quantifying mass transfer depends upon the reliability of the method of scaling δ_c . The results of this study suggest that these difficulties may be overcome by

focusing on the physical processes that control the DO transport more than simply using time-averaged DO microstructure data to estimate δ_c . Scaling δ_c using the Batchelor length scale yielded Sh values similar to the similarity model and bulk flux measurements, demonstrating that the surface-renewal and thin-film theories can agree when turbulence characteristics are quantified. New advances in the technology for characterizing fluid-flow (e.g., field PIV and ADV systems) allow for the estimation of properties such as bursting frequency, shear stress velocity, and energy dissipation near the sediments. The continued development of the eddy correlation method for aquatic systems (Berg et al. 2003) will allow for the simultaneous measurement of fluid-flow and DO at time-scales of interest to mass transfer. Inclusion of accurate fluid-flow and turbulence characterization is essential to further develop and verify models describing DO transfer to sediments.

References

- BERG, P., H. RØY, F. JANSSEN, V. MEYER, B. B. JØRGENSEN, M. HUTTEL, AND D. DE BEER. 2003. Oxygen uptake by aquatic sediments measured with a novel non-invasive eddy-correlation technique. *Mar. Ecol. Prog. Ser.* **261**: 75–83.
- BOGARD, D. G., AND W. G. TIEDERMAN. 1986. Burst detection with single-point velocity measurements. *J. Fluid Mech.* **162**: 389–413.
- BOUDREAU, B. P. 2001. Solute transport above the sediment–water interface, p. 104–126. *In* B. P. Boudreau and B. B. Jørgensen [eds.], *The benthic boundary layer: Transport processes and biogeochemistry*. Oxford Univ. Press.
- CAMPBELL, J. A., AND T. J. HANRATTY. 1983. Turbulent velocity fluctuations that control mass transfer to a solid boundary. *AiChE J.* **29**: 215–221.
- DANCKWERTS, P. V. 1951. Significance of liquid-film coefficients in gas absorption. *Ind. Eng. Chem.* **43**: 1460–1467.
- DWORAK, R., AND H. WENDT. 1977. Stochastic fluctuations of mass transport through turbulent boundary layers. *Berichte der Bunsen-Gesellschaft Phyk. Chem.* **81**: 864–869.
- GARCÍA, M., Y. NIÑO, AND F. LÓPEZ. 1996. Laboratory observations of particle entrainment into suspension by turbulent bursting, p. 63–86. *In* P. J. Ashworth, S. J. Bennett, J. L. Best, and S. J. McLelland [eds.], *Coherent flow structures in open channels*. Wiley.
- GUNDERSEN, J. K., AND B. B. JØRGENSEN. 1990. Microstructure of diffusive boundary layers and the oxygen uptake of the sea floor. *Nature* **345**: 604–607.
- GÜSS, S. 1998. Oxygen uptake at the sediment–water interface simultaneously measured using a flux chamber method and microelectrodes: Must a diffusive boundary layer exist? *Estuar. Coast. Shelf Sci.* **46**: 143–156.
- HONDZO, M. 1998. Dissolved oxygen transfer at the sediment–water interface in a turbulent flow. *Water Resour. Res.* **34**: 3525–3533.
- , T. FEYAERTS, R. DONOVAN, AND B. L. O'CONNOR. 2005. Universal scaling of dissolved oxygen distribution at the sediment–water interface: A power law. *Limnol. Oceanogr.* **50**: 1667–1676.
- JØRGENSEN, B. B., AND B. P. BOUDREAU. 2001. Diagenesis and sediment–water exchange, p. 211–244. *In* B. P. Boudreau and B. B. Jørgensen [eds.], *The benthic boundary layer: Transport processes and biogeochemistry*. Oxford Univ. Press.
- , AND D. J. DES MARAIS. 1990. The diffusive boundary layer of sediments: Oxygen microgradients over a microbial mat. *Limnol. Oceanogr.* **35**: 1343–1355.
- , AND N. P. REVSBECH. 1985. Diffusive boundary layers and the oxygen uptake of sediments and detritus. *Limnol. Oceanogr.* **30**: 111–122.
- KATUL, G., G. KUHN, J. SCHIEDGE, AND C. HSIEH. 1997. The ejection-sweep character of scalar fluxes in the unstable surface layer. *Boundary-Layer Meteorol.* **83**: 1–26.
- LAZIER, J. R., AND K. H. MANN. 1989. Turbulence and the diffusive layers around small organisms. *Deep-Sea Res.* **36**: 1721–1733.
- LORKE, A., B. MÜLLER, M. MAERKI, AND A. WÜEST. 2003. Breathing sediments: The control of diffusive transport across the sediment–water interface by periodic boundary-layer turbulence. *Limnol. Oceanogr.* **48**: 2077–2085.
- LUZNIK, L., R. GURKA, W. A. M. NIMMO SMITH, W. ZHU, J. KATZ, AND T. R. OSBORN. 2007. Distribution of energy spectra, Reynolds stresses, turbulence production, and dissipation in a tidally driven boundary layer. *J. Phys. Oceanogr.* **37**: 1527–1550.
- NAKAGAWA, S., AND T. J. HANRATTY. 2003. Influence of a wavy boundary on turbulence: ii. Intermediate roughened and hydraulically smooth surfaces. *Exp. Fluids* **35**: 437–447. doi:10.1007/s00348-003-0682-1.
- NEZU, I., AND H. NAKAGAWA. 1993. Turbulence in open-channel flows. *IAHR Monograph*, Balkema.
- NISHIHARA, G. N., AND J. D. ACKERMAN. 2007. On the determination of mass transfer in a concentration boundary layer. *Limnol. Oceanogr.: Methods* **5**: 88–96.
- PINCZEWSKI, W. V., AND S. SIDEMAN. 1974. A model for mass (heat) transfer in turbulent tube flow: Moderate and high Schmidt (Prandtl) numbers. *Chem. Eng. Sci.* **29**: 1969–1976.
- POPE, S. B. 2000. *Turbulent flows*. Cambridge Univ. Press.
- PRECHT, E., U. FRANKE, L. POLERECKY, AND M. HUETTEL. 2004. Oxygen dynamics in permeable sediments with wave-driven pore water exchange. *Limnol. Oceanogr.* **49**: 693–705.
- PROBSTEIN, R. F. 1989. *Physicochemical hydrodynamics*. Butterworths.
- ROBINSON, S. K. 1991. Coherent motions in the turbulent boundary layer. *Annu. Rev. Fluid Mech.* **23**: 601–639.
- RØY, H., M. HUTTEL, AND B. B. JØRGENSEN. 2002. The role of small-scale sediment topography for oxygen flux across the diffusive boundary layer. *Limnol. Oceanogr.* **47**: 837–847.
- , ———, AND ———. 2004. Transmission of oxygen concentration fluctuations through the diffusive boundary layer overlying aquatic sediments. *Limnol. Oceanogr.* **49**: 606–692.
- SHAW, D. A., AND T. J. HANRATTY. 1977. Turbulent mass transfer rates to a wall for large Schmidt numbers. *AiChE J.* **23**: 28–37.
- STEINBERGER, N., AND M. HONDZO. 1999. Diffusional mass transfer at sediment–water interface. *J. Environ. Eng.* **125**: 192–200.
- TENNEKES, H., AND J. L. LUMLEY. 1972. *A first course in turbulence*. MIT Press.
- WALSH, G. E., D. E. WEBER, L. K. ESRY, M. T. NGUYEN, AND J. N. B. ALBRECHT. 1992. Synthetic substrata for propagation and testing of soil and sediment organisms. *Pedobiologia* **36**: 1–10.
- WESTERWEEL, J. 1997. Fundamentals of digital particle image velocimetry. *Meas. Sci. Technol.* **8**: 1379–1392.

Received: 28 March 2007
Amended: 16 October 2007
Accepted: 22 October 2007